The International Journal of Advanced Manufacturing Technology (2021) 115:2581–2593
https://doi.org/10.1007/s00170-021-07297-8

ORIGINAL ARTICLE

Effects of CeO2 addition on microstructure and properties of ceramics reinforced Fe-based coatings by laser cladding

Liaoyuan Chen [1,2] · Yu Zhao [1,2] · Chuang Guan [1,2] · Tianbiao Yu [1,2]

Received: 19 May 2020 / Accepted: 17 May 2021 / Published online: 27 May 2021

Abstract

To reduce deposition defects (cracks and porosity) of the ceramics reinforced Fe-based coatings, and improve their microstructure uniformity, microhardness, and wear resistance, different content of CeO_2 (0, 1.0, 2.0, 2.5, and 3.0 wt.%) was added to the Fe-based powders. The effects of CeO_2 addition on the microstructure, phase composition, and mechanical properties were investigated by an optical microscope, X-ray diffraction (XRD), scanning electron microscopy (SEM), Vickers hardness tester, and friction wear tester. The results show that appropriate CeO_2 addition not only can reduce the cracks and porosities but also improve the bonding performance between the composite coating and the substrate. The study also finds that the addition of CeO_2 promotes the melting of large-size ceramic particles, increases the nucleation sites, and further refines the microstructure. The mechanical properties of each coating show that the microhardness and wear resistance firstly increases and then decreases with the increase of CeO_2 addition. The ceramics reinforced Fe-based coatings with 2.5 wt.% CeO_2 addition exhibites the highest and most uniform microhardness, and the smoothest worn surface despite the higher friction coefficient. Thus, CeO_2 addition is an effective method to refine the microstructure, reduce cracks and porosities in the TiN and Ti (C, N) reinforced Fe-based coating, and further improve microhardness and wear performance.

Keywords Laser cladding; · Fe-based coating; · CeO_2; · Ceramic phases; · Microstructure; · Mechanical properties

1 Introduction

Laser cladding technology (LCT) is one of the most commonly used additive manufacturing (AM) technology for metal materials in the industry, which applies a high-energy laser beam to add molten precursors on the substrate surface. Compared with other surface modification processes (such as plasma thermal spraying, surface carburizing or nitriding, surface welding, etc.), LCT has the advantages of low dilution rate, limited heat affected zone, and wide material adaptability [1–3]. Since Iron (Fe) or Fe-based alloy has the advantages of rich content, low cost, mature manufacturing process, and excellent compatibility with commonly used steel and cast iron parts, it is widely carried on surface repair or modification of worn or corroded waste parts over the years [4–6]. However, the low hardness and poor wear resistance of a single Fe-based powder are difficult to meet the requirements of mechanical properties of the part under the working conditions of high strength, heavy load, and high wear rate. A large number of studies have found that composite coatings with reinforcing phases as the hard phases, and metals or alloys as the binding phases exhibit excellent mechanical properties such as high wear resistance, hardness, and good corrosion resistance.

At present, the ceramics reinforced phases in Fe-based composite coatings are mainly carbide ceramics and nitride ceramics. WC is commonly used as carbide-reinforced ceramic [7, 8]. The addition of WC in low-hardness alloy coatings

✉ Tianbiao Yu
tianbiaoyudyx@gmail.com

Liaoyuan Chen
chen1910113@163.com

Yu Zhao
zhaoyuneu@gmail.com

Chuang Guan
guanchuang10193@163.com

[1] School of Mechanical Engineering and Automation, Northeastern University, Shenyang 110819, China

[2] Liaoning Provincial Key Laboratory of High-end Equipment Intelligent Design and Manufacturing Technology, Shenyang 110819, China

could greatly improve the microhardness and wear resistance, but the pores and cracks were prone to appear in the coatings with the WC content increasing [9, 10]. Wu et al. [11] investigated the phase evolution and corrosion behavior of SiC addition on laser cladding deposition of 316L stainless steel composites. The results show that the addition of SiC significantly refines the microstructure of the solidified metal matrix composites, the microhardness significantly increases from 362 to 974 HV, and the corrosion resistance is also improved. The micro-cracks are also observed in this study when the SiC content reaches 16 wt.%. Nitride ceramics are also a common ceramics reinforcing phase in the composite coatings. Liu et al. [12] prepared Ni-based h-BN composite lubrication coatings by both CO_2 and YAG laser. The microhardness is significantly improved and the main phases in coatings were composed of CrB, Ni_3B, Cr_7C_3. Results indicate that the crystals at the bottom of the coating are coarse and directional compared with the equiaxed crystal at the top and middle of the coating. Sun et al. [13] found that TiN reinforced Sialon composites had good toughness and tribological properties in a wide temperature range, and the fracture toughness of Sialon composites is effectively enhanced due to the addition of TiN.

Previous studies also found that the addition of ceramics phases would reduce the fluidity of liquid metal in the molten pool, lead segregation of alloy elements, and inhomogeneous microstructures, so cracks and porosities were prone to appear. Heat treatment [3, 14], optimization of the scanning strategy [15, 16], and the addition of non-metal or metal compounds [11, 17] are commonly used to reduce the segregation of the element composition and reduce the cracks and porosities. However, the heat treatment process would affect the microstructure of the substrate, especially in limiting the application of the surfacing repair process [18]. Optimizing the scanning strategy could often reduce porosities and cracks in the overlap area, but have a limited effect on the phase composition of the coating [19, 20]. Therefore, the addition of a small amount of metal or nonmetal compounds has a positive significance to improve the overall performance of the ceramics reinforced coating. Rare earth elements are surface-active substances, which can reduce the melting point of alloy systems, increase the nucleation rate, and purify impurities. Tao et al. [21] added La_2O_3 to the WC ceramics reinforced Ni-based coatings with high corrosion and wear resistance. The study found that a small number of rare earth elements can accelerate the dissolution of WC particles and improve surface smoothness. The addition of the La_2O_3 have promoted the refinement of the microstructure, and increased the microhardness and wear resistance [22]. Besides, adding a small amount of Y_2O_3 to Ti6Al4V powder could refine the microstructure by transforming α-titanium grains from cellular crystals to equiaxed crystals, improved the microhardness and reduced cracking sensitivity of the coating. Therefore, rare earth elements can significantly reduce the microporous structure and refine the microstructure of the overlap zone of the coating, which is conducive to improving the microhardness and wear resistance [23–25].

A further requirement for the ceramics reinforced composite coatings fabricated by LCT is that the coating not only exhibits high microhardness and excellent wear resistance but also has no cracks, porosities, and other defects. In previous studies on improving the performance of Fe-based coatings, the addition of ceramics tends to increase the sensitivity of cracks and porosities of coatings. To solve the above problems, in this study, the effects of CeO_2 addition on the cracks, porosities, microstructure, microhardness, and wear resistance of the coating were investigated and discussed in detail based on the successful preparation of ceramics reinforced composite coating. We hope that the results of this study would improve the overall mechanical performance of the ceramics reinforced composite coatings, and further promote its industrial application.

2 Experimental details

The Fe-based self-fluxing powder with ceramics addition (7.00 wt.% Ti, 21.00 wt.% TiN, 1.80 wt.% C) and different of CeO_2 contents (0, 1.0, 2.0, 2.5, and 3.0 wt.%) were selected as the precursors. The chemical composition of the Fe-based self-fluxing powder and substrate are shown in Table 1. The SEM image and particle size statistics of the Fe-based powder are shown in Fig. 1. The average diameter of Ceria (CeO_2) with 99.9 wt.% purity is 32 nm. The chemical compositions of the precursors for coating are listed in Table 2. The mass of each component was weighed by an electronic balance (accuracy 0.01 mg), and the precursors were mixed in a planetary mixer for 3 h at 400 r/min. Before the experiment, the precursors should be dried for 4 h in a drying cabinet with a constant temperature of 100 °C.

The equipment for this study is an integrated laser cladding system (see in Fig. 2), which is mainly composed of a KUKA robot (KR16-2), controller, laser generator (wavelength 1020 nm, maximum power 500W), a cladding head (RC52), powder feeder, and workbench. The powder and laser transfer system are integrated into the cladding head, which is mounted at the end of the A6 axis of the KUKA robot. The program was written and optimized by the offline programming software (RobotArt) and imported into the controller, which controlled the scanning path, the switch of the laser power, powder feeder, and shielding gas. The coating with two layers was fabricated by LCT. The distance between the two tracks is 0.56 mm, and the z-axis increment is 0.47 mm. The scanning path was always along the x-axis during the LCT process, which meant that the scanning directions in the two adjacent tracks were opposite. The shielding gas and

Table 1 Chemical compositions of Fe-based powder and the substrate

Element (wt.%)	C	Cr	Si	Ni	B	Mn	Cu	P	Fe
Fe-based powder	0.1-0.2	14-18	1.0-1.5	2.0-2.5	1.0-2.0	0.2-0.5	-	-	Bal.
Substrate	0.42-0.50	≤0.2	0.17-0.37	≤0.30	-	0.50-0.80	≤0.25	≤0.035	Bal.

carrier powder gas were Argon (purity 99.99%). The optimized process parameters are shown in Table 3 according to our previous study [26].

The preparation process for test samples is shown in Fig. 3. Each coating was cut into two samples along section-A by a wire electric discharge machine. Section-A of the sample 1# was ground by sandpaper and polished according to the standard metallographic method, and then were etched with self-contained chemical etching solution (25 ml HCl, 25 ml H_2O, and 5 g $FeCl_3$) for 10 s. Finally, the sample 1# was subsequently cleaned ultrasonically. The scanning electron microscopy (SEM, Zeiss, Germany) equipped with an energy-dispersive spectrometer (EDS) was used to observe the microstructure and obtain the chemical composition of each phase. The microhardness on the section-A of coatings was measured by HV-1000 Vickers microhardness tester (HV-1000, China) with a load of 500 gf and applied for 10 s along the growth direction, at 100 μm equidistant point. The top surface of sample 2# was ground, and polished by hand to obtain a flat plane B for X-ray diffraction (XRD) analysis and then wear tests. The parameters for the XRD (Pertpro, Netherlands, measurement accuracy, 2θ±0.01°) with Cu Kα radiation were the diffraction angle with 10° to 90° and the scanning time of 10 min. The wear performance of coatings was carried on the material surface property tester (MFT-4000, China). The direction of the friction pair was consistent with the scanning direction, as shown in Fig. 3. To avoid unnecessary experimental errors, three wear experiments were performed at different positions on plane B. The wear parameters are shown in Table 4. The results of representative experiments were used as the object of wear performance analysis. The wear volume was calculated by Eq. 1 [26]. As shown in Fig. 4, R is the radius of the wear ball ZrO_2. The L and B are the length and width of wear tracks, respectively, which are measured by an Olympus laser confocal microscopy (OLS4000, Japan). The worn surface morphologies of the different coating were also observed by Olympus laser confocal microscopy.

$$V = \left[R^2 \arcsin\left(\frac{B}{2R}\right) - \left(\frac{B}{2}\right)\sqrt{R^2 - \left(\frac{B}{2}\right)^2}\right] \cdot L \quad (1)$$

Table 2 Compositions of the cladding precursors (wt.%)

Coating number	Composite powder	CeO_2
1	100	0
2	99.0	1.0
3	98.0	2.0
4	97.5	2.5
5	97.0	3.0

3 Results and discussion

3.1 Cross-sectional morphology

Previous studies have shown that the enormous differences in thermal expansion coefficient between in-situ ceramics and matrix ([Fe-Cr] solid solution) would lead to large stress and further result in cracks in the composite coating during laser cladding [27–29]. Figure 5 shows the SEM images of composite coatings with different content of CeO_2 addition. The addition of CeO_2 has an obvious effect on the cross-section morphology of the coating. As shown in Fig. 5(a), the bonding performance between coating 1 and substrate without CeO_2 addition is poor, and the cracks are mainly distributed near the bonding line. Meanwhile, many pores are also found. The existence of previous precipitates prevented some pores from being filled by liquid during the solidification and shrinkage process, so pores were formed [29, 30]. As shown in Fig. 5(b), compared with coating 1 without CeO_2 addition, almost no porosities and cracks in coating 2 are reduced, while the number of cracks near the bonding line is increased. This phenomenon may be attributed to two aspects. On the one hand, laser cladding is a typical non-equilibrium phase transition process, which is characterized by rapid melting and solidification of the cladding material. Therefore, the liquid phase was bound by the surrounding solidified matrix during the cooling shrinkage process, resulting in tensile stress, and excessive tensile stress would release cracks [31, 32]. Because of the good heat dissipation of the substrate, big cracks were more likely to be generated near the bonding line. On the other hand, the added Ce could be used as a surface activation element to form stable low-melting compounds with slag-forming elements such as B and Si in MLPs. These compounds would take away the gas in the coating during the

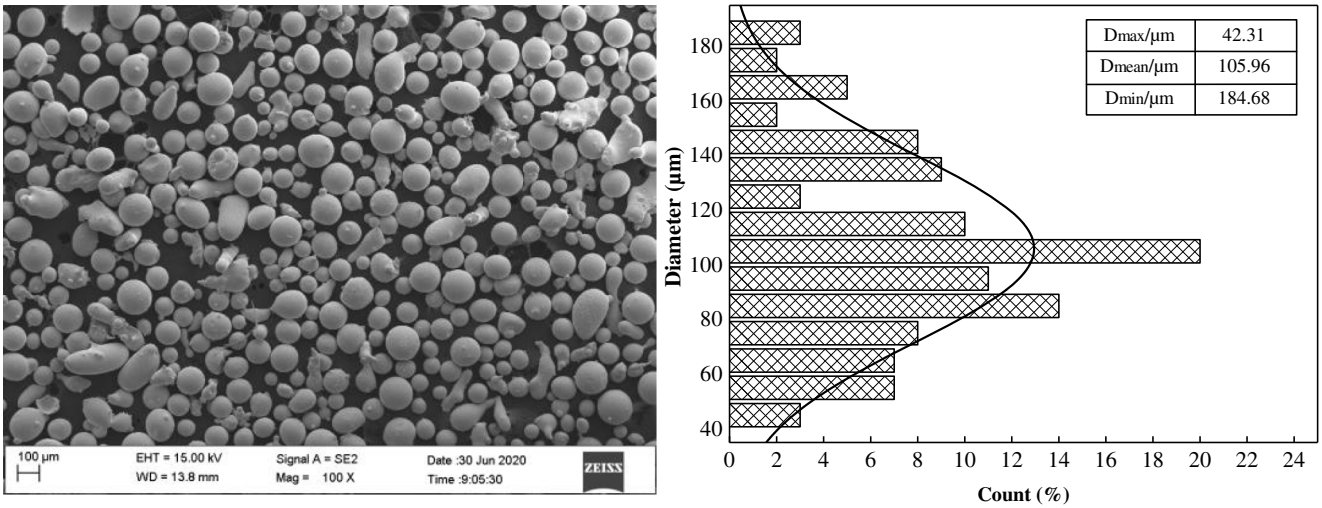

Fig. 1 The SEM image and particle size statistics of the Fe-based powder

floating process, which reduced the component segregation, purified the microstructure, and increased the fluidity of liquid alloy, resulting in the reduction of pores in the coating. When the content of CeO_2 is 2.0 wt.%, as shown in Fig. 5(c), the inner cracks are small, and the number of porosities also decreases. While the number of cracks near the bonding line is significantly reduced, when the CeO_2 addition is increased to 2.5 wt.%, as shown in Fig. 5(d1), the number of cracks and porosities in coating 4 is the least the microstructure is uniformly distributed, and the cracks through the whole coating are not found. Figure 5 (d2) represents an enlarged SEM image at the interface of coating 4, and no step behavior of microstructure is observed in the metallurgical bonding zone between coating and substrate, which is beneficial to the subsequent machining and service of the coating. When the CeO_2 addition increases to 3.0 wt.%, as shown in Fig. 5(e), although there is no obvious segregation between the coating and the substrate, internal cracks run through the entire coating, and the porosities also increase. In general, the addition of excessive CeO_2 increased the number of impurity compounds, which could significantly reduce the convection phenomenon. Therefore, a large number of these unexpected compounds were retained in the coating during the solidification process. Due to the large surface roughness, the bonding ability between the coating and the substrate is poor, and the crack-sensitive zone was formed here. With further solidification, the large tensile stress caused by rapid cooling was easy to act on these crack-sensitive zones, resulting in the formation of large cracks. Besides, the porosity also increased due to the untimely shrinkage of the liquid with poor fluidity during the solidification process.

3.2 Phase analysis

The XRD patterns for each coating with different CeO_2 addition are shown in Fig. 6. The highest diffraction peaks of the [Fe-Cr] solid solution are observed in all composite coatings, which indicates that composite coatings are mainly composed of [Fe-Cr] solid solution due to their largest mass fraction in the precursors. Besides, some diffraction peaks of Ti (C, N) and TiN are also found in Fig. 6. During the laser cladding process, the precursor powders were heated and melted to form Fe-Ti-N-C multicomponent liquid phases (MLPs) by laser energy, and then rapidly solidified, which would lead to complex physical and chemical reactions. Combining the XRD results, the potential reaction in the cladding process can be as follows [33, 34]:

$$\mathrm{Ti} + \mathrm{C} \rightarrow \mathrm{TiC} \quad (2)$$

$$\mathrm{TiN} + \mathrm{C} \rightarrow \mathrm{Ti(C,N)} \quad (3)$$

$$\mathrm{TiC} + \mathrm{TiN} \rightarrow \mathrm{Ti(C,N)} \quad (4)$$

Table 3 Optimized process parameters for Fe-based powder

Parameters	Values
Laser power	450 W
Scanning speed	0.70 mm/s
Powder feeding rate	0.65 r/min
Carrier powder gas	8.0 L/h
Shielding gas	15 L/h

Due to the low negative Gibbs free energy and the high melting point (3140 °C) of TiC, it tended to precipitate from the MLPs without considering the solute concentration. Since the time of laser action on the precursors is very short (even less than 0.2 s), it is difficult for some large-size TiN to be completely melted (see in Fig. 7a1). Therefore, some C atoms infiltrated into the TiN edge, which promoted the occurrence of reaction 3 and formed Ti (C, N) solid solution [35]. Since

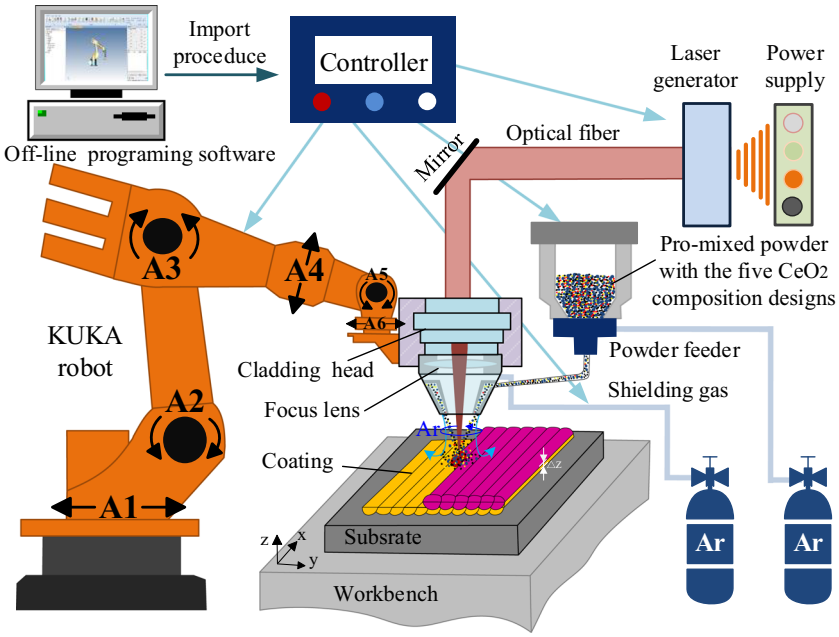

Fig. 2 Laser cladding system

both TiC and TiN are face-centered cubic lattice structure, they are easy to dissolve each other to form a "zero-dimensional" ternary solid solution Ti(C, N). It should be noted that the CeO_2 addition has little effect on the phase composition of the composite coating. However, some different diffraction peaks of composite coating with different CeO_2 addition are found on the left side of the diffraction peak of [Fe-Cr] solid solution. Figure 6 indicates that the diffraction peak of unexpected TiC phase is found in the coatings 1–3. This phenomenon might be caused by the insufficient convection in the MPLs, which led to the insufficient time of the interaction between TiC and TiN. CeO_2 would be decomposed into Ce and O elements after it reached the melting point (3500°C) under the action of laser energy. The decomposed Ce is a kind of surface-active element, which can reduce the surface tension and free energy, so it can promote the inward flow of MLPs [36]. This behavior promoted the high-temperature liquid flow to the interior of the MLPs, the decomposition of TiN, and further improved the uniformity of the element distribution. Therefore, during solidification, this phenomenon increased the probability and dwell time of the contact between the TiN and in-situ TiC, which improved the content of Ti (C, N). As shown in Fig. 6, when the CeO_2 content is 2.5 wt.%, no TiC is found in the coating 4. Since Ce was easy to form compounds with slagging elements such as B and Si, excess CeO_2 (more than 2.5 wt.%) would lead to the formation of a large number of compounds in the MLPs, and they were difficult to float the coating. A large number of compounds reduced the convection. As a result, some C elements are difficult to be consumed to form TiC in coating 5. XRD results show that the appropriate addition of CeO_2 can promote the formation of the reinforcement Ti (C, N) phases, which is beneficial to improve the microhardness and wear properties of the coatings.

Table 4 Wear test process parameters

Parameters	Values
Friction pair	Φ5 mm ZrO_2
Samples size (mm^3)	15×15×10
Load (N)	10
Wear time (min)	30
Reciprocating distance (mm)	6
Sliding speed (mm/min)	220
Temperature (°C)	25 ± 1

3.3 Microstructure

Figure 7 shows the SEM microstructure at the middle of the composite coating with different content of CeO_2 addition. The addition of CeO_2 has an obvious effect on the shape and size of the microstructure of the coating. All coatings are mainly composed of the dendrite or equiaxed crystal, and their color is mainly white, gray, and dark gray. EDS was carried out to confirm the chemical composition of each phase, and results are shown in Fig. 8. Since the A1 is composed of Fe, Cr, a small amount of C, and no N elements, the white dendrites crystal can be identified as [Fe-Cr] solid solution. Figure 8(b) indicates that the elements in the gray phase inside the columnar structure are mainly Ti and N elements, and the content of the C element is more than that in the white dendrites crystal, and the atomic ratio of Ti, N, and C is close to 2:1:1. According to reports [29, 37] and combined with

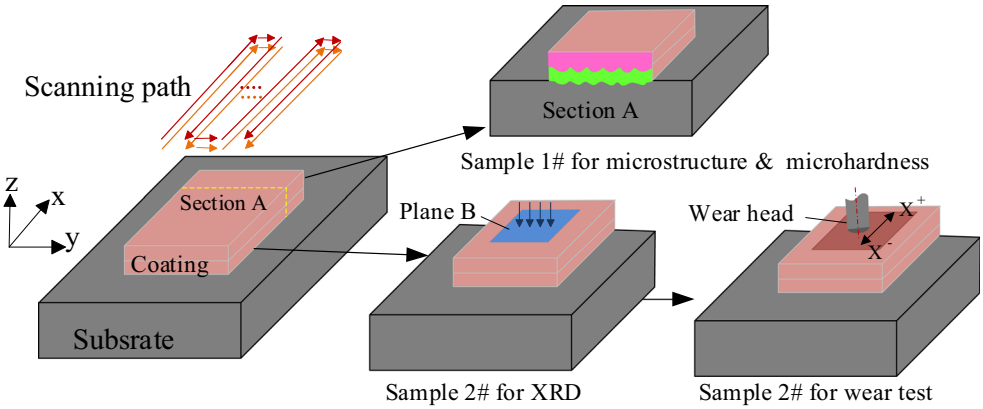

Fig. 3 The preparation process of coating test samples

XRD results, A2 with a similar shape and composition can be considered as Ti (C, N). A3 is the refined equiaxed crystal, which is mainly composed of Fe, Cr, and C elements. The dark gray component analysis results of the central region of the columnar structure are shown in Fig. 8(d). Compared to A2, the content of the C element is increased, while the content of the Ti element and N element is decreased. The A4 can also be considered as Ti (C, N). According to the results of spectral analysis, it is found that with the increase of the C content, the color of the microstructure in the coating changed from white to gray, and dark gray. The components of locally distributed gray and dark gray phases are mainly Ti (C, N).

As shown in Fig. 7(a1, a2), the microstructure in coating 1 is dominated by coarse dendrites with large Primary Dendrite Arm Spacing (PDAS), and locally distributed fine grains. At the same time, large unmelted TiN particles were also found. On the one hand, it is difficult for large TiN with a high melting point (2950 °C) to be completely melted due to the short time of laser acting on the precursors. On the other hand, the heat source with Gaussian distribution led to a large *G* on the surface of MLPs, resulting in uneven distribution of surface tension and flow of metal liquid [34, 35]. The larger *G* is beneficial to the growth of coarse dendrite. At the same time, the addition of TiN would hinder the flow of metal liquid and further reduce flow velocity. This phenomenon would lead to the decrease of the solute diffusion of decrease the MLPs, resulting in insufficient melting of TiN. Figure 7(b1, b2) shows that the distribution and size of columnar crystals in coating 2 are more uniform than that in coting 1 without CeO_2 addition, and no unmelted TiN was found. As revealed earlier,

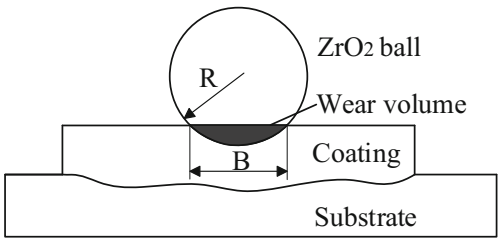

Fig. 4 Schematic diagram of the cross-section of wear track

rare earth easily reacted with impurities elements (S, O, B, Si, etc.) to form high-melting compounds in MLPs [38]. Under the influence of convection, these compounds were separated from the MLPs in the form of slag and then floated from the metal liquid before solidification [14]. Therefore, the molten pool was purified after desulfurization and deoxidation, and the inclusions were reduced. This phenomenon improved the convection of metal liquid and increased its flow velocity. These effects could accelerate the melting rate of TiN, so no unmelted TiN particles are found in the coating with the CeO_2 addition. Figure 6 (c1, c2) represents the microstructure of coating 3 with 2.0 wt.% CeO_2 addition. It can be found that compared with coating 2, enhancement of CeO_2 addition reduces the number and size of micro-cracks, and further improve the compactness of the coating. As shown in region H of Fig. 7(c1), the tails of the two dendrites are connected by an equiaxed crystal, which increases the uniformity of the microstructure. Given the high melting point of CeO_2, the unmelted CeO_2 particles could be used as heterogeneous nucleation points at the beginning of solidification, which played a needle effect during the solidification process and further refined the microstructure. Therefore, the columnar crystal decreased, the number of equiaxed grains increased, and the uniformity of the internal structure of the coating was further improved. These phenomena indicate that the CeO_2 can not only increase the fluidity of liquid metal and reduce the component undercooling during solidification but also reduce the segregation of the component. Therefore, the microstructure of the coating tends to be uniform. When the content of CeO_2 addition increases to 2.5 wt.%, the microstructure in coating 4 is mainly equiaxed crystals with uniform distribution, and there are only a few dendrites, as shown in Fig. (d1, d2). During the solidification process, the growing crystals would be hindered by the rare earth Cerium gathered at the boundary of the crystal. This behavior reduced the Gibbs free energy of the whole metal alloy system and increased the driving force required for crystals growth, reduced the segregation of solidified microstructure [38–40]. Therefore, the PDAS in coating 4 is decreased. To reveal the distribution of main elements in coating

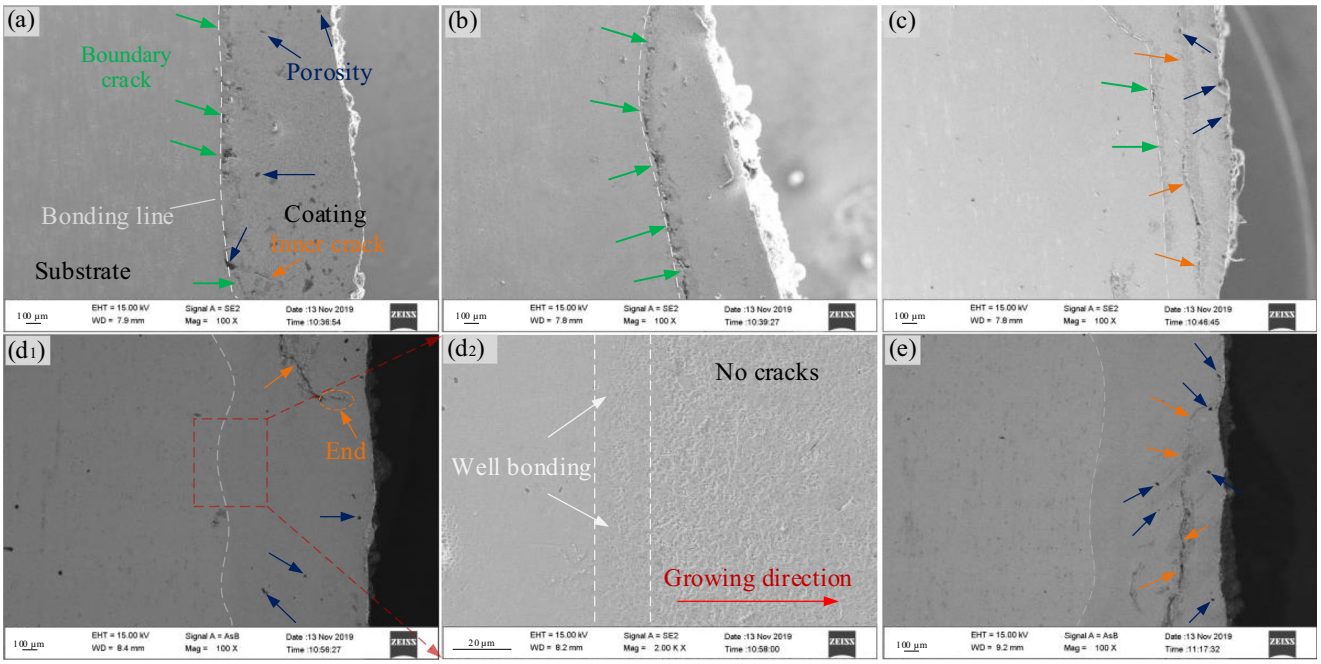

Fig. 5 SEM images of coating with different CeO_2 addition: (a) coating 1; (b) coating 2; (c) coating 3; (d) coating 4; (e) coating 5

4, EDS mapping scanning was carried out, and the results are shown in Fig. 9. It can be seen from Fig. 9(b) that the Fe, Ti, C, and N elements are uniformly distributed in coating 4, and there is no enrichment phenomenon. The dark gray phases are mainly Ti, N elements, and a very small number of C elements, which can be identified as ceramics phases (Ti(C, N) and TiN) combined with the XRD results. When the CeO_2 content is 3.0 wt.%, the microstructure of the composite coating 5 is shown in Fig. 6(e1, e2). Since the first ionization energy of rare earth elements was very small, the Cerium atoms with easily polarized valence electrons could easily combine with other atoms, which would form a stress field. The microstructure in the coating is easy to agglomerate, and the precipitation of the ceramic phases is hindered due to the excessive CeO_2 addition. Therefore, the increase of dendrite crystals, the large PDAS, and the decrease of equiaxed crystals are observed in the coating 5. The excessive CeO_2 addition is not beneficial to the refining microstructure.

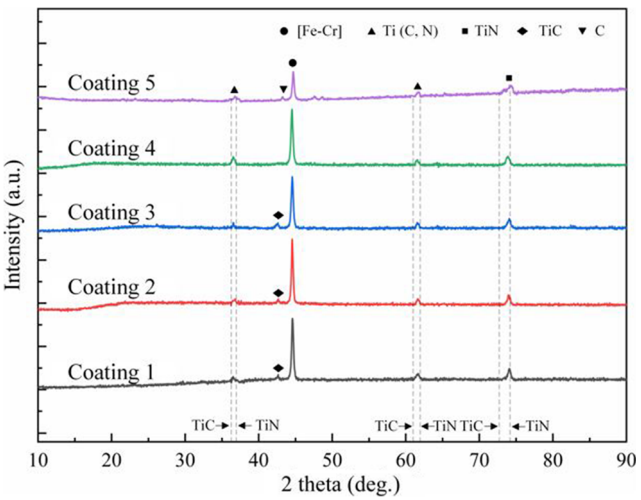

Fig. 6 X-ray diffraction patterns from each coating

3.4 Microhardness

Microhardness is one of the important indicators for evaluating coating performance. The indentation position and corresponding measurement results are shown in Fig. 10(a). The average microhardness profits of different coatings are shown in Fig. 10(b). It can be noticed that the average microhardness of coating 1 without CeO_2 addition is the lowest of 623.33 HV. The average microhardness of the coatings with 1.0, 2.0, 2.5, and 3.0 wt.% CeO_2 addition correspond 639.16 HV, 659.04 HV, 709.46 HV, and 644.68 HV, respectively. The obvious increase of hardness can be explained by the fine-grain strengthening effect and the relatively dense hard phases. On the one hand, the composite coating with CeO_2 addition has a more uniform grains distribution and smaller size (see Fig. 7), so the grain number in the unit volume is greatly increased. The coating with fine grains can show excellent resistance to the external load, which improves the microhardness and achieves fine grain strengthening. On the other hand, rare earth elements can promote the precipitation of C, B, Cr from the MLPs to form carbide and boride hard phases, which is beneficial to improve the mechanical properties of the coating. However, excessive CeO_2 would lead to the aggregation of precipitates, resulting in the formation of coarse crystals and further reducing microhardness. To analyze the effect of CeO_2 addition on the microhardness

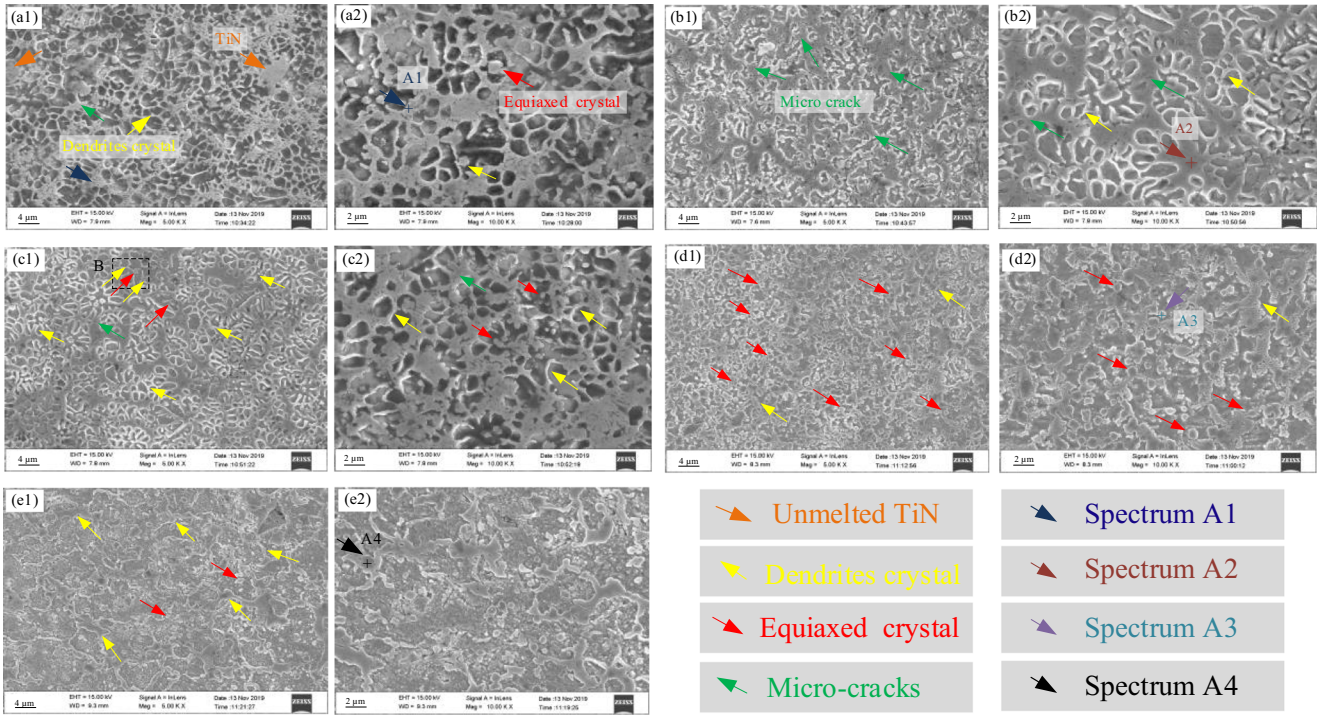

Fig. 7 SEM microstructure of the coatings with different CeO_2 contents at different magnification: (a1-2) coating 1; (b1-2) coating 2; (c1-2) coating 3; (d1-2) coating 4; (e1-2) coating 5

distribution in the coating, the standard deviation of the microhardness in different coatings was obtained. The standard deviation analysis results of the effect of CeO_2 addition on microhardness are shown in Fig. 10. As the amount of CeO_2 addition increases, the standard deviation of microhardness decreases firstly and then increases. When CeO_2 addition is 2.5 wt.%, the standard deviation of the microhardness of coating 4 is the smallest, which means that the microhardness distribution in the coating is the most uniform. This is related to the homogeneous distribution of hard phases and microstructure due to CeO_2 addition. The trend of the microhardness means that CeO_2 addition has an effective effect on the microhardness of the coating.

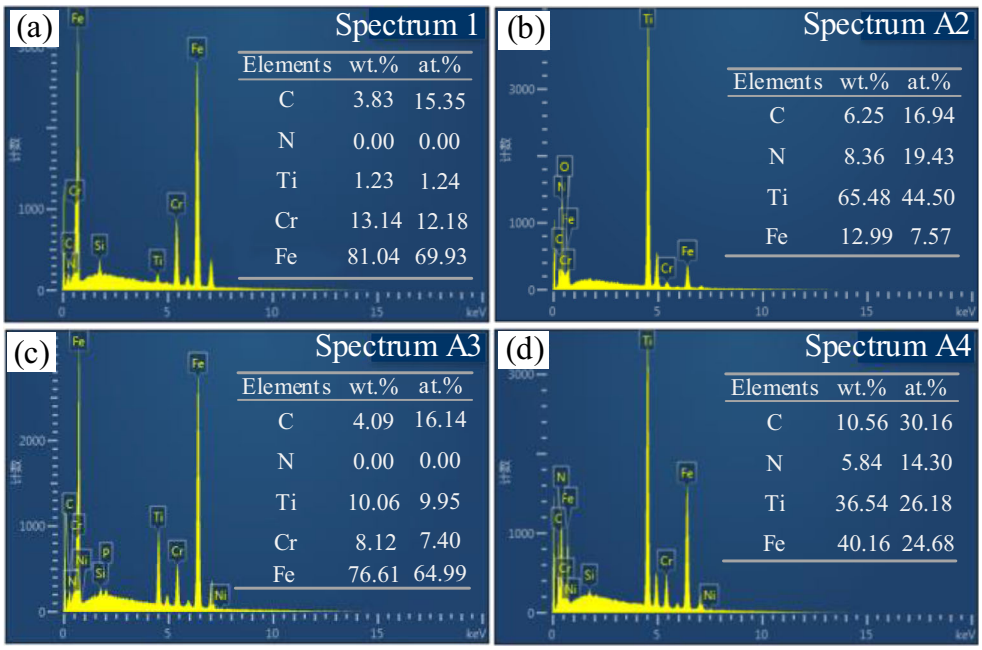

Fig. 8 The EDS spectra obtained from different phases in Fig. 7

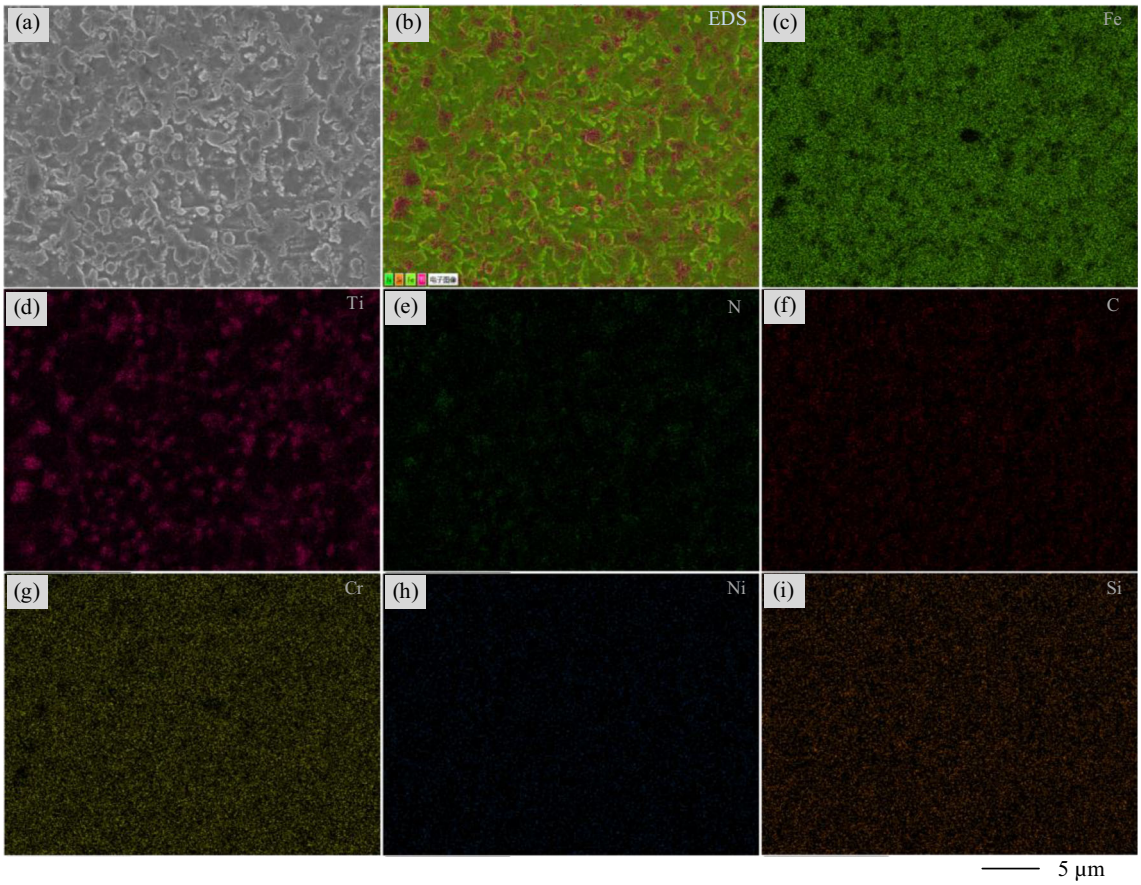

Fig. 9 SEM analysis for the element distributions of Fe, Ti, N, C, Cr Ni, and Si from coating 4

3.5 Wear properties

To explore the effect of CeO_2 addition on the wear properties of the composite coating, dry sliding experiments were carried out. Figure 11 illustrates that the friction coefficient versus sliding time of the composite coating with different CeO_2 addition has the same trend. At the beginning of the sliding process, the friction coefficient is small because the polished surface has low roughness. As the sliding time increases, the worn head was pressed into the coating, and the material on the coating surface was gradually removed, resulting in a gradual increase in friction coefficient. About 10 min later, the friction coefficient of each coating tends to be stable. It can be seen from the local enlarged image of the friction coefficient that the friction coefficient in the stable stage of the coating without CeO_2 addition has the largest fluctuation.

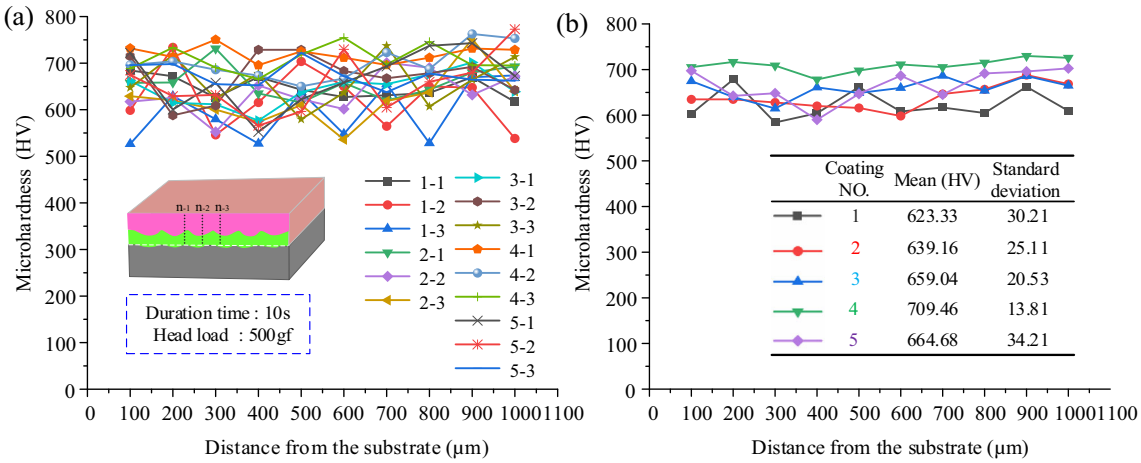

Fig. 10 Micro-hardness distribution along the growth direction: (a) test position and corresponding microhardness, (b) average microhardness of each composite coating

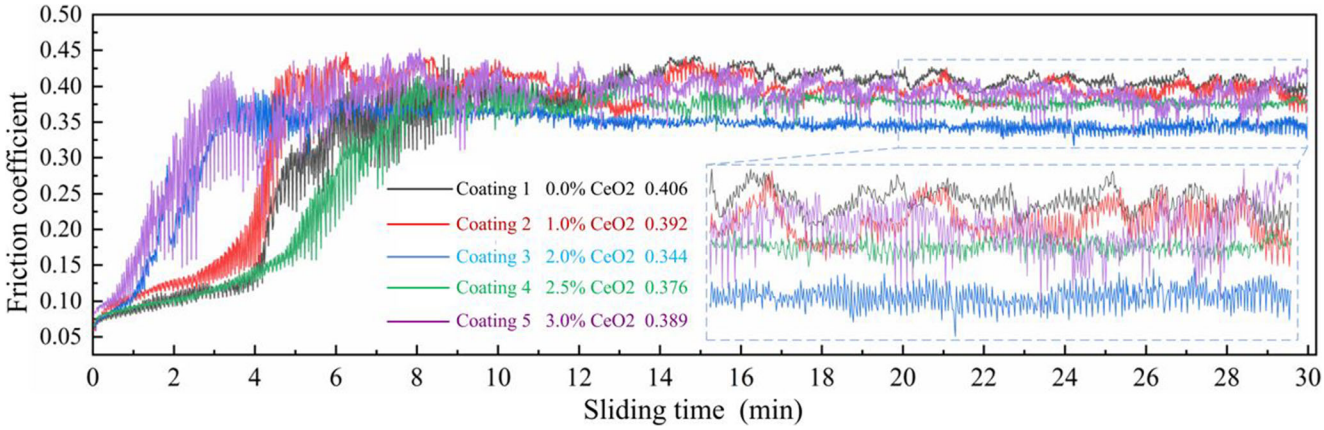

Fig. 11 Friction coefficient of different coatings versus sliding time

When the CeO_2 addition is 2.5 wt.%, the friction coefficient is the smoothest among all coatings. The average value of the friction coefficient during the last 10 min of stabilization is determined as the friction coefficient of each coating. Wear volume and friction coefficient of the different coatings are shown in Fig. 12. As the content of CeO_2 increases, the friction coefficient of the coating decreases firstly and then increases. It can be seen from the friction coefficient curve that an appropriate amount of CeO_2 addition is beneficial to reduce the friction coefficient. The coating without the CeO_2 addition has the highest friction coefficient which is over 0.4. When the CeO_2 addition is 2.0 wt.%, the friction coefficient of the coating is the smallest of 0.344, and the wear volume loss is the least (11.3226 μm^3). It should be noted that the wear volume of each coating with different CeO_2 addition corresponds to their friction coefficient. This indicates that these coatings may have the same wear mechanism. These results show that appropriate CeO_2 addition can significantly improve the wear properties of the coating.

The worn surface of each coating was observed by laser confocal microscopy to explore the wear mechanism. Figure 13 shows the two-dimensional (2D) and three-dimensional (3D) worn surfaces of different coatings. It is found from Fig. 13(a1-2) that the spalling behavior of the material on surface of the coating 1 is serious, and the surface morphology is inhomogeneous, which results in a large fluctuation of the friction coefficient (see Fig. 11). During the process of repeated sliding process, cracks would gradually expand under the action of alternating stress and eventually result in large-area spalling on the surface. The wear mechanism of coating 1 may be fatigue wear. Therefore, coating 1 shows poor wear performance. Figure 13(b1-2) represents the worn surface of coating 2 is smoother compared with coating 1, and the surface spalling of the material changes from a large region to some local small regions. This is mainly due to the addition of CeO_2 to reduce the defects of the coating (see Fig. 5) and improve the bonding force between the hard phases and the matrix. Therefore, during the sliding process, the hard phases in the coating were not easy to peel off in large quantities and irregularly. It is found from Fig. 13(c1-2 and d1-2) that with the increase of the CeO_2 addition, the large regions of material palling on the surface of the coating are reduced, and the convex height and concave depth of the coating are lower than those of other coatings. Especially on the worn surface of coating 4, the furrow scratches are effectively refined. When the rare earth addition is less than 3.0 wt.%, the microstructure is indeed refined. This results in the grain boundary having enough capacity to carry the load, which is beneficial to promote stress relaxation during the sliding process, increase the resistance of crack propagation, and then reduce the number of cracks. At the same time, the dislocation ability of the grain boundaries increases, the plastic deformation ability of the coating is also improved. Therefore, the probability of brittle fractures and spalling are reduced, and the smooth region is increased. However, when the excess CeO_2 is added to the composite coating, the number of cracks and abrasive debris on the worn surface of the coating 5 increase, and the smooth regions are greatly decreased. Too much rare earth oxide would accumulate at the grain boundary, which could hinder the movement of dislocation, improve

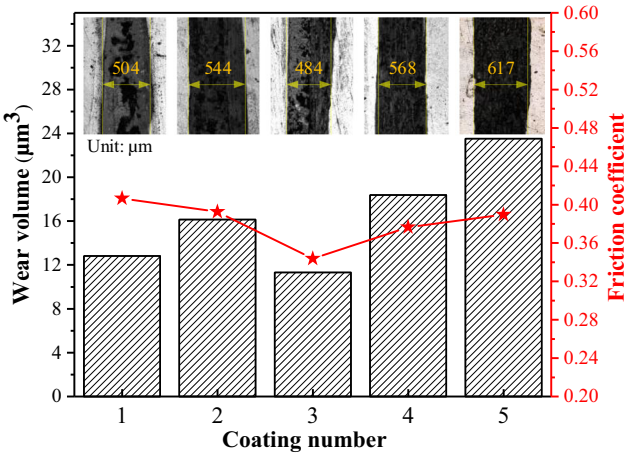

Fig. 12 Wear volume and friction coefficient of the different coatings

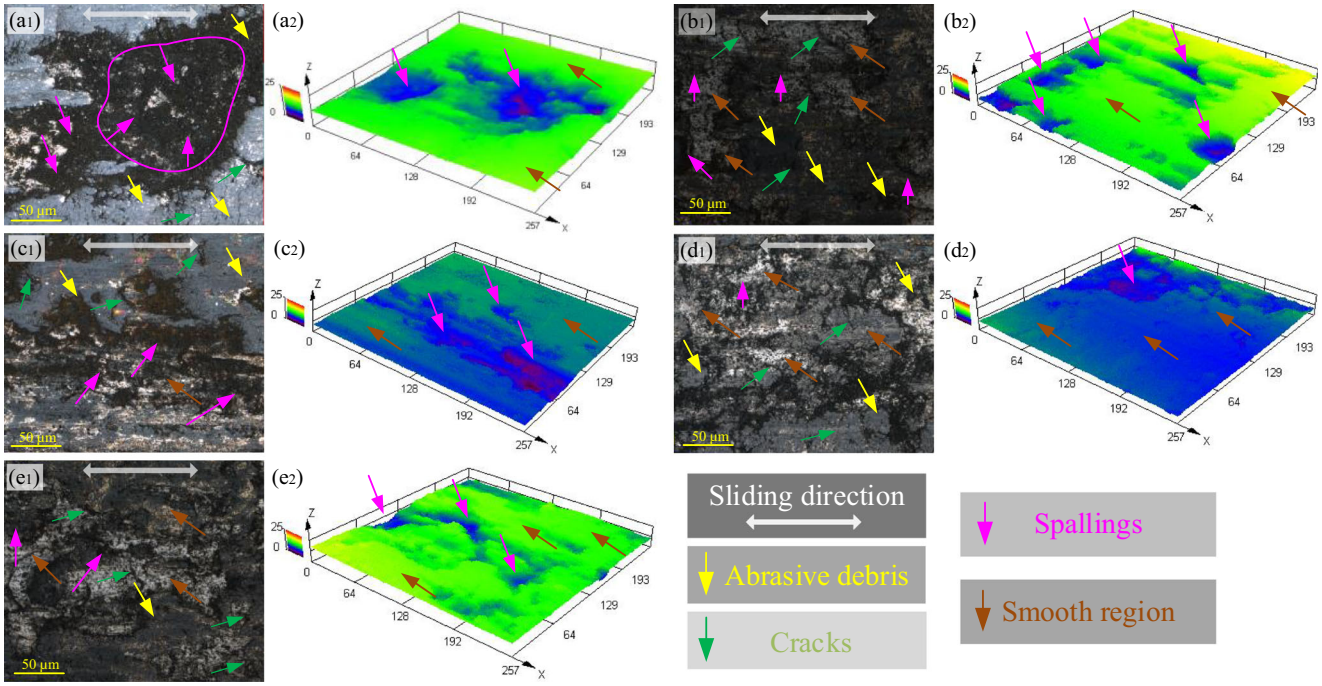

Fig. 13 The 2D and 3D worn surfaces of (a1-2) coating 1; (b1-2) coating 2; (c1-2) coating 3; (d1-2) coating 4; (e1-2) coating 5

the brittleness of the grain boundary and increase the number of cracks. The space of ceramics phase dislocation was reduced during the sliding process, and the probability of occurrence of chipping and fracture was greatly increased, thereby aggravating the wear.

4 Conclusions

In this work, different components of CeO_2 were added to the precursors with Fe-based powder and ceramics particles to refine the microstructure and improve the mechanical properties of the composite coating by laser cladding. The effects of CeO_2 content on phase composition, microstructure distribution, microhardness, and wear properties of the ceramics reinforced composite coating were systematically studied in detail. The conclusions obtained from this study can be drawn:

1. The addition of CeO_2 effectively weakens the penetrating cracks in the coating and reduces the sensitivity of cracks and porosities. Thus, the compactness of the microstructure in the coating is also improved.
2. The addition of CeO_2 promotes the melting of the added ceramic phases, which is beneficial to the formation of the expected Ti (C, N). Adding an appropriate amount of CeO_2 weakens the growth direction of microstructure, increases the nucleation sites, and further promotes the transformation from dendrite to equiaxed crystal.
3. The composite coating with 2.5 wt.% CeO_2 addition shows the highest microhardness of 709.46 HV and the lowest standard deviation, which is mainly caused by fine grain strengthening and promoting the formation of hard phases.
4. The wear resistance of the coating with 2.0 wt.% CeO_2 addition is better than that of the other coating. The improvement of wear resistance is contributed to the solution strengthening and grain boundary strengthening due to CeO_2 addition.

Acknowledgements This work was supported in part by the Fundamental Research Funds for the Central Universities (N2003026).

Data availability The data and materials that support the findings of this study can be shared upon request. All data generated or analyzed is presented within the study itself.

Declarations

Consent to participate The authors have informed consent.

Conflict of interest The authors declare no competing interests.

References

1. Shamsaei N, Yadollahi A, Bian L, Thompson SM (2015) An overview of Direct Laser Deposition for additive manufacturing; Part II: Mechanical behavior, process parameter optimization and control. Addit Manuf 8:12–35. https://doi.org/10.1016/j.addma.2015.07.002
2. Pi G, Zhang A, Zhu G, Li D, Lu B (2011) Research on the forming process of three-dimensional metal parts fabricated by laser direct

metal forming. Int J Adv Manuf Technol 57:841–847. https://doi.org/10.1007/s00170-011-3404-5
3. Ibrahim MZ, Sarhan AAD, Kuo TY, Yusuf F, Hamdi M, Chien CS (2018) Investigate the effects of the substrate surface roughness on the geometry, phase transformation, and hardness of laser-cladded Fe-based metallic glass coating. Int J Adv Manuf Technol 98:1977–1987. https://doi.org/10.1007/s00170-018-2354-6
4. Song L, Zeng G, Xiao H, Xiao X, Li S (2016) Repair of 304 stainless steel by laser cladding with 316L stainless steel powders followed by laser surface alloying with WC powders. J Manuf Process 24:116–124
5. Ozlati A, Movahedi M (2018) Effect of welding heat-input on tensile strength and fracture location in upset resistance weld of martensitic stainless steel to duplex stainless steel rods. J Manuf Process 35:517–525
6. Liu H, Li M, Qin X, Huang S, Hong F Numerical simulation and experimental analysis of wide-beam laser cladding. Int J Adv Manuf Technol 100:237–249
7. Lo KH, Cheng FT, Kwok CT, Man HC (2003) Improvement of cavitation erosion resistance of AISI 316 stainless steel by laser surface alloying using fine WC powder. Surf Coat Technol 165:258–267
8. Farahmand P, Kovacevic R (2015) Laser cladding assisted with an induction heater (LCAIH) of Ni-60%WC coating. J Mater Process Technol 222:244–258. https://doi.org/10.1016/j.jmatprotec.2015.02.026
9. Guo C, Chen J, Zhou J, Zhao J, Wang L, Yu Y, Zhou H (2012) Effects of WC-Ni content on microstructure and wear resistance of laser cladding Ni-based alloys coating. Surf Coat Technol 206:2064–2071. https://doi.org/10.1016/j.surfcoat.2011.06.005
10. Qu J, Xiong W, Ye D, Yao Z, Liu W, Lin S (2010) Effect of WC content on the microstructure and mechanical properties of Ti(C0.5N0.5)-WC-Mo-Ni cermets. Int J Refract Met Hard Mater 28:243–249. https://doi.org/10.1016/j.ijrmhm.2009.10.005
11. Wu CL, Zhang S, Zhang CH, Zhang JB, Liu Y, Chen J (2019) Effects of SiC content on phase evolution and corrosion behavior of SiC-reinforced 316L stainless steel matrix composites by laser melting deposition. Opt Laser Technol 115:134–139. https://doi.org/10.1016/j.optlastec.2019.02.029
12. Liu S, Shin YC (2017) The influences of melting degree of TiC reinforcements on microstructure and mechanical properties of laser direct deposited Ti6Al4V-TiC composites. Mater Des 136:185–195. https://doi.org/10.1016/j.matdes.2017.09.063
13. Sun Q, Wang Z, Yang J, Liu Y, Liu J, Qiao Z, Liu W (2018) High-performance TiN reinforced Sialon matrix composites: A good combination of excellent toughness and tribological properties at a wide temperature range. Ceram Int 44:17258–17265
14. Yin J, Wang D, Meng L, Ke L, Hu Q, Zeng X (2017) High-temperature slide wear of Ni-Cr-Si metal silicide based composite coatings on copper substrate by laser-induction hybrid cladding. Surf Coat Technol 325:120–126
15. Yu T, Sun J, Qu W, Zhao Y, Yang L (2018) Influences of z-axis increment and analyses of defects of AISI 316L stainless steel hollow thin-walled cylinder. Int J Adv Manuf Technol 97:2203–2220
16. Zhang S, Lin X, Chen J, Huang W (2009) Heat-treated microstructure and mechanical properties of laser solid forming Ti-6Al-4V alloy. Rare Metals 28:537–544. https://doi.org/10.1007/s12598-009-0104-5
17. Yu T, Zhao Y, Sun J, Chen Y, Qu W (2018) Process parameters optimization and mechanical properties of forming parts by direct laser fabrication of YCF101 alloy. J Mater Process Technol 262:75–84
18. Casati R, Lemke J, Vedani M (2016) Microstructure and Fracture Behavior of 316L Austenitic Stainless Steel Produced by Selective Laser Melting. J Mater Sci Technol 32:738–744. https://doi.org/10.1016/j.jmst.2016.06.016
19. Zhao Y, Yu T, Li B, Wang Z, Chen H (2018) Calculation and verification of start/stop optimum overlapping rate on metal dlf technology. Int J Adv Manuf Technol 99:437–452. https://doi.org/10.1007/s00170-018-2445-4
20. Zhao Y, Yu T, Li B, Wang Z, Chen H (2018) Effect of laser cladding on forming qualities of YCF101 alloy powder in the different lap joint modes. Int J Adv Manuf Technol 96:1991–2001
21. Tao Z, Xun C, Shunxing W, Shian Z (2000) Effect of CeO2 on microstructure and corrosive wear behavior of laser-cladded Ni/WC coating. Thin Solid Films 379:128–132
22. Sharma SP, Dwivedi DK, Jain PK (2009) Effect of La2O3 addition on the microstructure, hardness and abrasive wear behavior of flame sprayed Ni based coatings. Wear 267:853–859
23. Li J, Yu ZS, Wang HP (2011) Effects of Y2O3 on Microstructure and Mechanical Properties of Laser Clad Coatings Reinforced by In Situ Synthesized TiB and TiC. Mater Sci Forum 675–677:589–592
24. Choi JO, Kim JY, Choi CO, Kim JK, Rohatgi PK (2004) Effect of rare earth element on microstructure formation and mechanical properties of thin wall ductile iron castings. Mater Sci Eng A 383:323–333
25. Hao F, Li D, Dan T, DAN T, REN X, LIAO (2011) Effect of rare earth oxides on the morphology of carbides in hardfacing metal of high chromium cast iron. J Rare Earths 29:168–172. https://doi.org/10.1016/S1002-0721(10)60425-5
26. Yu T, Yang L, Zhao Y, Sun J, Li B (2018) Experimental research and multi-response multi-parameter optimization of laser cladding Fe313. Opt Laser Technol 108:321–332. https://doi.org/10.1016/j.optlastec.2018.06.030
27. Yan H, Zhang P, Gao Q, Qin Y, Li R (2017) Laser cladding Ni-based alloy/nano-Ni encapsulated h-BN self-lubricating composite coatings. Surf Coat Technol 332:422–427. https://doi.org/10.1016/j.surfcoat.2017.06.079
28. Yoon S, Kim J, Kim BD, Lee C (2010) Tribological behavior of B4C reinforced Fe-base bulk metallic glass composite coating. Surf Coat Technol 205:1962–1968. https://doi.org/10.1016/j.surfcoat.2010.08.078
29. Zhao Y, Yu T, Guan C, Sun J, Tan X (2019) Microstructure and friction coefficient of ceramic (TiC, TiN and B4C) reinforced Ni-based coating by laser cladding. Ceram Int 45:20824–20836. https://doi.org/10.1016/j.ceramint.2019.07.070
30. DebRoy T, Wei HL, Zuback JS, Mukherjee T, Elmer JW, Milewski JO, Beese AM (2018) Additive manufacturing of metallic components – Process, structure and properties. Prog Mater Sci 92:112–224. https://doi.org/10.1016/j.pmatsci.2017.10.001
31. Zhang Z, Huang Y, Rani Kasinathan A, Imani Shahabad S, Ali U, Mahmoodkhani Y, Toyserkani E (2019) 3-Dimensional heat transfer modeling for laser powder-bed fusion additive manufacturing with volumetric heat sources based on varied thermal conductivity and absorptivity. Opt Laser Technol 109:297–312
32. Wei S, Wang G, Shin YC, Rong Y (2018) Comprehensive modeling of transport phenomena in laser hot-wire deposition process. Int J Heat Mass Transf 125:1356–1368. https://doi.org/10.1016/j.ijheatmasstransfer.2018.04.164
33. Yang L, Yu T, Li M, Zhao Y, Sun J (2018) Microstructure and wear resistance of in-situ synthesized Ti(C, N) ceramic reinforced Fe-based coating by laser cladding. Ceram Int 44:22538–22548. https://doi.org/10.1016/j.ceramint.2018.09.025
34. Yanan L, Ronglu S, Wei N, Tiangang Z, Yiwen L (2019) Effects of CeO_2 on microstructure and properties of TiC/Ti2Ni reinforced Ti-based laser cladding composite coatings. Opt Lasers Eng 120:84–94
35. Zhao Y, Yu T, Chen L, Chen Y, Guan C, Sun J (2020) Microstructure and wear resistance behavior of Ti–C–B_4C-reinforced composite coating. Ceram Int 46:25136–25148. https://doi.org/10.1016/j.ceramint.2020.06.300

36. Zhao J, Wang G, Wang X, Luo S, Wang L, Rong Y (2020) Multicomponent multiphase modeling of dissimilar laser cladding process with high-speed steel on medium carbon steel. Int J Heat Mass Transf 148:118990. https://doi.org/10.1016/j.ijheatmasstransfer.2019.118990
37. Yin Z, Yan S, Xu W, Yuan J (2018) Microwave sintering of Ti(C, N)-based cermet cutting tool material. Ceram Int 44:1034–1040
38. Wang KL, Zhu YM, Zhang QB, Sun ML (1997) Effect of rare earth cerium on the microstructure and corrosion resistance of laser clad-ded nickel-base alloy coatings. J Mater Process Technol 63:563–567. https://doi.org/10.1016/S0924-0136(96)02684-2
39. Qi X, Zhu S (2015) Effect of CeO_2 addition on thermal shock resistance of WC–12%Co coating deposited on ductile iron by electric contact surface strengthening. Appl Surf Sci 349:792–797
40. Cai Y, Luo Z, Chen Y, Ao S (2017) Influence of CeO_2 on tribological behaviour of TiC/Fe-based composite coating. Surf Eng 33:936–943